THz Near Field Focusing using a 3D Printed Cassegrain Configuration for Backscattered Side-Channel Detection

Sinan Adibelli, Prateek Juyal, Chia-Lin Cheng, and Alenka Zajic, *Senior Member, IEEE*

***Abstract*— This paper presents the use of THz near field focusing for backscatter side channel detection. Near field focusing is done by using cassegranian reflector configuration. The focuser is designed to produce the focused beam 28 cm away from the antenna aperture. The focusing is done in the near field region by axially moving the subreflector from the focal point. It is observed that the subreflector position has to shift approximately 11 wavelengths along the axis to create the focus at the required location. The focused antenna gain is 46 dBi while the 3 dB focus width and depth of the designed antenna is ~ 4 mm and 10 cm, respectively. It is found that the focal plane position is sensitive to the subreflector shifts and it is observed that 1 mm change in the subreflector position can shift the focal plane by ~ 2 cm. The simulations are compared with measurement results of a fabricated prototype and good agreement is observed. The antenna is fabricated by using 3D printing technology, which allows rapid prototyping. Finally, we have demonstrated the detection of backscatter side channel from the board placed at 28 cm away from the designed antenna. The received power level of the backscatter signal increases by 6 dB as compared to horn antenna.**

***Index Terms*— EM side channel, Near field Focusing, THz Signals, Reflector Antennas**

I. Introduction

Side-channel analysis has emerged as a powerful tool for data theft, especially in the context of breaking encryption in commercial implementations. These attacks exploit the fact that encryption implementations on physical devices transfer much more information than just the desired input-output information [1]. Side-channel attacks circumvent traditional access control and protection by exploiting the observable side effects of computation rather than attacking the computation's functionality. Computations have many observable side effects through analog mediums such as power consumption [1], [2], [3], sound [4], [5], and electromagnetic (EM) emanations [6], [7], [8], [9], [10], [11] that can be exploited to create side-channel attacks.

On the other hand, side-channels have also been used for detecting malicious activities both in software (e.g. detecting malware [12] [13] [14] [15] [16]) and in hardware (e.g. Trojan detection [17], [18]). More recently, new backscattering side-channel has been discovered and leveraged for Trojan detection and RFID communications [19].

All previous work on EM side-channels has been focused on low-MHz range frequencies, i.e., 1-10 MHz. More recently, researchers have been investigating GHz range frequencies [15], [16] for side-channel monitoring and exploring a new type of side-channel based on backscatter signals created by switching transistors inside microprocessors [19].

The high frequency of THz signals has great advantage over GHz range signals for side-channel detection in terms of bandwidth and noise/interference. The large (at least 20 GHz) useful bandwidth of THz backscattering provides tens of signal points per nanosecond, which is sufficient to provide information not only about switching activity from one cycle to another, but also within the cycle, which can provide important information about software and hardware activity via side-channels that was not available before. Also, microwave range has a lot of strong sources of interference such as AC power, AM, FM, and satellite radio, cellular phone, etc., while these sources of interference are not present at THz frequencies. Another benefit of monitoring side-channels at THz frequencies is that beam can be focused on smaller part of the processor, not on the whole chip as it is case at lower frequencies. This will also significantly improve hardware Trojan detection. To receive these THz backscattering signals at a distance from the emanating board, focused spot beams or high directivity antennas, are required.

In this paper, to receive the emanated backscattered signals at a distance greater than 20 cm from the board, THz near field focusing is used, which is achieved by a novel near field antenna configuration. It is shown in the paper that the side channel can be detected 28 cm away from the board. Near field focusing is done in the past using different antenna structures. For instance, the near field focusing at the microwave frequencies is done by various different approaches which includes hybrid structures using substrate integrated waveguide SIW technology [20], Fresnel zone plate [21], [22]; microstrip [23], [24]; and reflect array antennas [25], [26]. At THz frequencies, near field focusing is demonstrated in the past [27], [28], [29] , [30]. In the planar antennas, small size of the patch element poses various fabrication challenges, which leads to expensive fabrication techniques such as electron beam

This work has been supported, in part, by NSF grants 1651273 and 1740962 and ONR grant N00014-17-1-2540. The views and findings in this paper are those of the authors and do not necessarily reflect the views of NSF or ONR.

The authors are with Electrical Engineering Department, Georgia Institute of Technology, Atlanta, USA

lithography, microfabrication. Here, we presents a novel silver-coated 3-D printed cassegrain reflector configuration for THz near field focusing. This is less expensive, allows rapid prototyping and has not been used earlier for the near field-focused reflectors. The particular metallization technique that was used, i.e., coating with silver paint, offers a faster and less expensive alternative to electroplating and 3D metal printing. The reason for the particular reflector configuration is based on our measurement set up to detect the backscatter channel. It has been established previously that at microwave frequencies the prime focus reflectors focus the beam when feed is axially displaced [31]. This technique is used here to design a dual reflector cassegranian configuration to achieve near field focusing at 300 GHz.

The rest of the paper is organized as follows. Section II describes the designed near field focusing apparatus. Section III analyzes the sensitivity of the design to reflector system to small shifts in the subreflector. Section IV presents simulation results and comparison with measurements. Section V presents how designed reflector can be used to focus EM side channel signals. Finally, Section VI concludes the paper.

II. Near Field Focused Antenna Design

This section presents the near field focusing using Cassegrain antenna system at 300GHz. THz frequency focusing using a dual reflector offset configuration with an ellipsoidal main reflector was shown in [32] for imaging and scanning applications. In general, ellipsoidal reflector configurations have been widely used for near field focusing. In our case, we selected cassegrain configuration with a paraboloid as main reflector since it can be easily converted into an optimal far field antenna (not discussed in this paper) using struts of corresponding lengths. Also for our case the main reflector size is 10cm, for which the profile of both elliptic and parabolic reflectors are approximately similar with a difference of $\lambda/20$ at the edges. This is clearly shown in Fig. 1 where the equation of the parabolic profile (selected for design) is $z = x^2/240$ and the equivalent elliptic profile for similar near field focus location is $\frac{(z-209)^2}{(209)^2} + \frac{x^2}{(160)^2} = 1$.

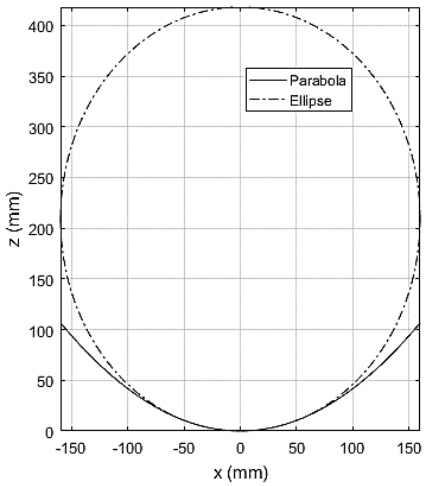

Fig. 1 Comparison of the parabolic and equivalent elliptic profile for main reflector

For larger main reflector sizes, say 30cm, the two profiles are different at the edges; hence using a parabolic profile can affect the near field focusing parameters. To confirm, for a diameter of 10 cm, we performed full wave simulations with both paraboloid and equivalent ellipsoid profile as main reflectors (secondary reflector profile remains same). The relative power densities along z-axis is shown in Fig. 2. The maximum power density region has similar location (difference is < 3%) along the axis, for both the profiles. For paraboloid reflector, the maximum power density is 0.35dB less than ellipsoid, which is acceptable in the present case as the parabolic configuration can be converted into far field antenna, with 0.35dB more gain as compared to ellipsoid reflector.

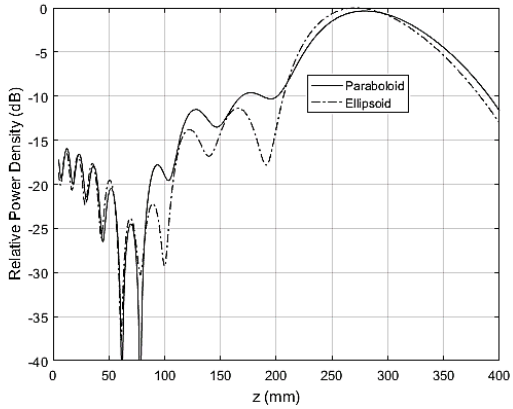

Fig. 2 Relative power density of the the paraboloid reflector and the equivalent ellipsoid reflector

The focusing antenna geometry is illustrated in Fig. 3. For the side-channel reception requirement, the focusing plane should be within the range of 25-35 cm from the antenna aperture. In other words, this represents the distance between the board or chip surface and the antenna aperture. Hence, focus depth of the designed antenna should be ~10cm. The chip surface on the board is a 2 cm X 2 cm square surface, the required focus width for the incident beam should be within 5 mm. This poses the limitation on the focus width. Ideally, the focal plane position of the focused antenna should coincide with the surface of the board. We started the design for the value of 28cm (i.e. the focal plane is at the 28 cm from the subreflector, as shown in Fig. 3)

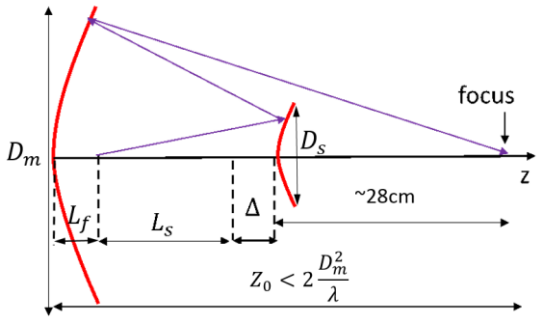

Fig. 3 Illustration of near field focusing in cassegrain configuration at 28 cm by shifting the subreflector from focal point by Δ.

It is well known that when the second focal point of

subreflector overlaps with the focal point of the main reflector, the beam is focused at infinity (in the far field). To focus the beam at a finite distance in the near field region, the subreflector needs to be shifted axially along z-direction away from the main reflector by Δ, as shown in the Fig. 3. This will result in focusing of the beam at Z_0, which is the distance from the main reflector vertex to the beam focus. Here, we choose the focal plane position to be 28 cm form the subreflector vertex and have main reflector size smaller than 10 cm X 10 cm X 10 cm (meaning the primary reflector diameter must be 10 cm). To focus the beam in the near field region, i.e. $Z_o < 2D_m^2/\lambda$, the feed should be displaced by more than $2(\mathrm{F/D_m})^2$ in wavelengths [33]. For the cassegrain configuration, the focusing is done by displacing the subreflector along the axis. It is known that to focus the antenna, a symmetric quadratic phase is required at the aperture [34]. The technique of shifting the subreflector is a straightforward way of achieving the desired phase distribution on the reflector. Equation (1) and (2) describes the parabolic and hyperbolic profile of the primary and secondary reflector respectively.

$$z = \frac{x^2}{4f_m} \tag{1}$$

$$\frac{z^2}{a_s^2} - \frac{x^2}{b_s^2} = 1 \tag{2}$$

Eccentricity and the magnification factor of a farfield cassegrain antenna is given in [35], where $f_e$is the focal length of the equivalent parabola, $2\psi_0$ is the subtended angle of the main reflector, and $2\theta_0$ is the effective subtended angle at the feed.

$$M = \frac{f_e}{f} \tag{3}$$

$$e = \frac{M+1}{M-1} \tag{4}$$

$$e = \frac{\sin\frac{1}{2}(\psi_0+\theta_0)}{\sin\frac{1}{2}(\psi_0-\theta_0)} \tag{5}$$

For the initial far-field design, the eccentricity and magnification are 1.63 and 4.2 respectively. For the near field design, the subreflector is shifted away from the focus by Δ, which results in a change in *M*. Equations (3)-(5) are defined for farfield Cassegrain reflectors. In case of a nearfield focus by shifting of the subreflector (without modifying the subreflector shape), due to a mismatch in foci locations, (3)-(5) will not give the correct magnification factor *M*. To calculate an accurate value of *M*, Gaussian optics can be used since the feed horn has a narrow beamwidth [36]. The dual reflector system in the near field focus configuration can be represented by two equivalent lenses as shown in Fig. 4. The magnification factor *M* is then obtained as

$$M = \frac{|f|}{\sqrt{(z-f)^2+z_0^2}}, \tag{6}$$

where z_0 is Rayleigh distance (equivalent of focus depth), and z is waist location (equivalent of focus location). The magnification factor was calculated using (6) and its variation with subreflector shift is discussed in Sec III.

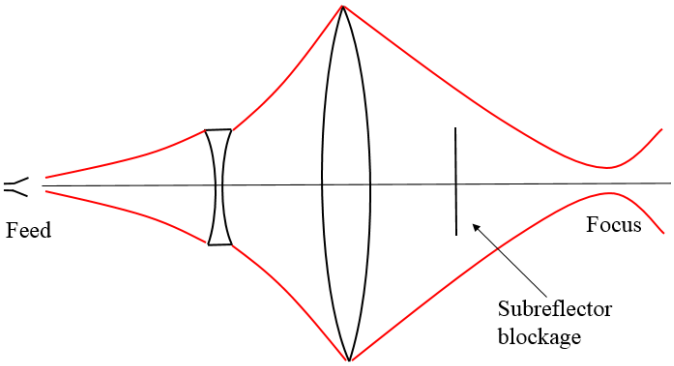

Fig. 4 Equivalent lens configuration of the near-field focused cassegrain dual reflector system.

The focus parameters are then calculated and compared with the full wave simulation results as shown in Fig. 14 of section III.

The cassegrain system was designed and simulated at 300GHz using CST's Integral Equation Solver (version 2017) [37]. Initially the far field antenna having a gain of 46 dBi was designed. The geometrical parameters for the design are listed in Table I.

Table I Design parameters for the focused antenna

D_m	100 mm	Primary reflector diameter
f_m	60 mm	Primary reflector focal length
D_s	15.7 mm	Secondary reflector diameter
a_s	14.36 mm	Secondary reflector hyperbola parameter
b_s	18.48 mm	Secondary reflector hyperbola parameter
L_f	5 mm	Feed point offset w.r.t. primary reflector vertex
L_s	45.95 mm	Distance between the feed and the vertex of the secondary reflector
Δ	13 mm	Amount of shift applied to the secondary reflector to bring the focus to the nearfield

Near field focusing at the required position is then achieved by moving the subreflector along the axis. For the focal plane position to be at 28 cm from the subreflector vertex, the shift Δ is 13 mm. To show the near field focusing, the simulated power densities for the designed near field focus antenna and the far field antenna were plotted and shown in Fig. 5. The power densities are plotted with the relative distance $r/(2D_m^2/\lambda)$ along the axis of the antenna. It is observed from the Fig. 5 that for the far field antenna, the power density is 46 dB higher than the isotropic radiator at a distance of $2D_m^2/\lambda$. This is also expected as the initial far field antenna has 46 dBi gain. In contrast, the near field cassegrain design has a very sharp peak in the near field. This peak is the focus of the designed antenna. Beyond this focal point, the power density decreases rapidly and falls below the power density of the far-field system as shown in the Fig. 5.

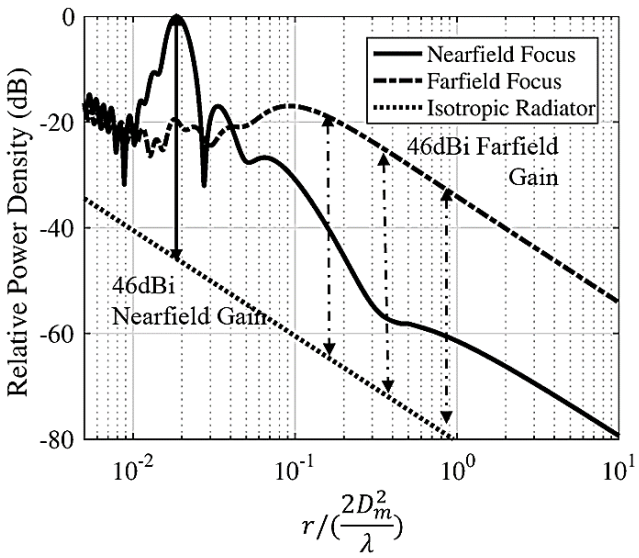

Fig. 5 Relative power densities of near field and far field focused systems compared to the ideal isotropic radiator.

In the far field dual reflector the peak directivity value depends upon secondary illumination. For near field focusing, shifting of the subreflector will change the illumination and corresponding edge taper values. To check this, the simulated relative power density vs the subreflector radius is shown in Fig. 6. The power density is shown for both the initial far field configuration and the near field design. It is pointed out that the edge taper changes from 9 dB to 5.4 dB, as the subreflector is shifted to achieve near field focusing. This is a relatively low edge taper as compared to the conventional value of 10 dB. This is due to the mechanical consideration of having to mount the entire reflector on the body of the diagonal horn places constraints on the location and the size of the subreflector. For these reasons, the design was found to be a good balance.

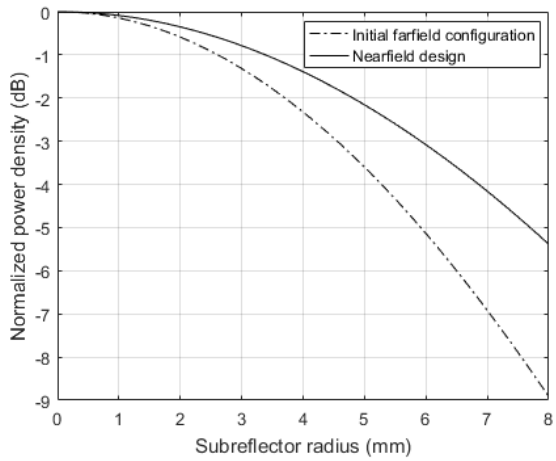

Fig. 6 Normalized power density values vs subreflector radius for the farfield and nearfield configurations on the surface of the subreflector.

To investigate the different properties of the focus, in Fig. 7 we show the 2D power density plot in the xz-plane. The subreflector vertex is at z=0 (i.e. the subreflector is placed between $-1.2\text{mm}<z<0\text{mm}$, since the subreflector is 1.2 mm thick) and the y-axis shows the 10 cm region spanned by the width of the primary reflector. Fig. 7 shows that the field is weak and spread at z=0 plane. However, as we move away from the subreflector, the field starts to concentrate around y = 0 and as it approaches the designed focal length of 28 cm, the field becomes very concentrated. Beyond this point, the field spreads out again, losing its effectiveness as a near field focused antenna. The focus spot in the focal plane of the antenna (z = 28cm) is shown in Fig. 8.

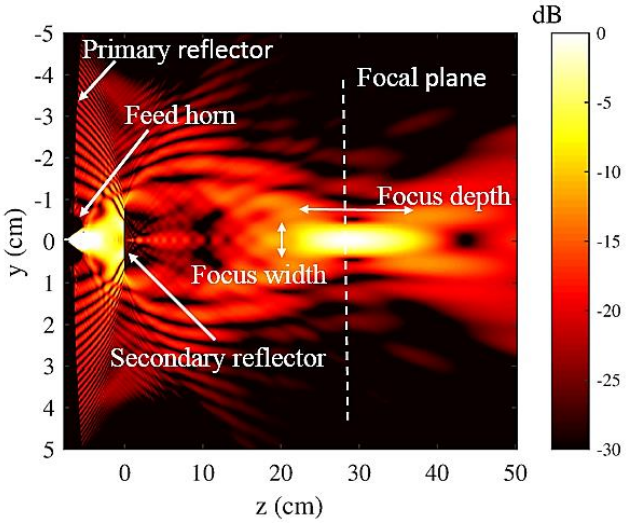

Fig. 7 Simulated 2D power density plot in xz-plane for the antenna geometry shown in Fig. 1

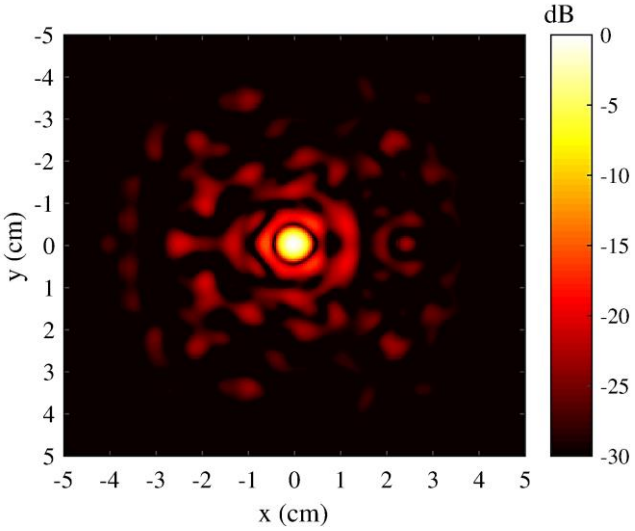

Fig. 8 Simulated 2D power density on the xy focal plane.

III. Focus Sensitivity

A. *Axial and lateral subreflector shift*

The designed reflector was used in the application presented in Section V, which involves measuring of the power emanated by the board placed at a distance from the designed antenna. The measurement setup is shown in Fig. 20. It is well known from the previous studies that as feed moves along the axis the main beam can be focused at a finite distance. At THz frequency range, the operating wavelengths are few mm and a small deviation in the subreflector position from the designed value can affect the focal parameters. It is possible that this

deviation can happen in the fabrication process. For this reason, in this section, we investigate in detail the sensitivity of the focus as a function of the position of the subreflector. The effect on various focus parameters such as focus width and depth, were investigated as the subreflector position changes. Along with the sensitivity, we also investigate the effect of the large subreflector shifts (up to 20λ) on the focus spot parameters. In the fabrication process, as explained later in Sec IV A, the subreflector is supported by the plastic struts (shown in Fig. 19). The sensitivity of the focus is investigated by plotting a positional error of the location of the subreflector. Defining the position error δ (the axial offset of the subreflector in reference to the designed near field focused subreflector position, shown in Fig. 9, where positive values of δ indicate a shift away from the main reflector), simulations were done for different δ values with a step size of 0.2 mm.

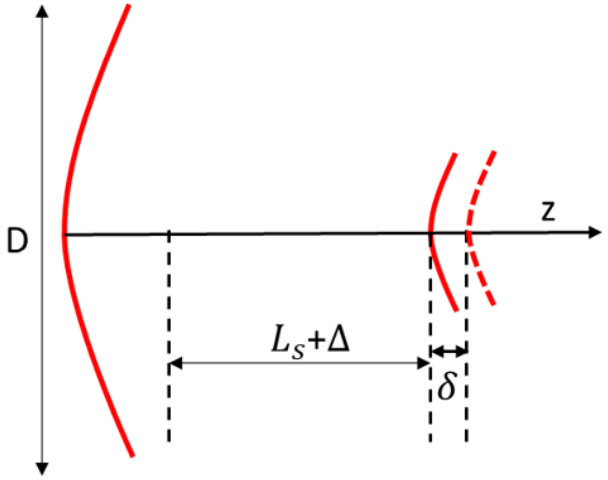

Fig. 9 Geometry showing small shift in the positioning of the subreflector δ.

Fig. 10 shows the change in the position of focus with the changes in the location of the subreflector. The manufactured prototype (corresponding to $\delta = 0$ mm) has a focal point at approximately 28 cm away from the antenna). As δ increases, the focal point moves closer to the antenna. As shown in the Fig. 10, for 2 mm change in the position of subreflector, the focal point position changes by 44 mm. This shows that even a few mm deviation in the subreflector position will change the focal plane position. Although the fabrication and the measurement procedure has been discussed in detail in Section IV, to validate the simulations, the measured position of the focus are also presented in the Fig. 10.

We do not analyze δ values greater than 25 mm because the focusing performance of the antenna degrades quickly beyond that point. As shown in Fig. 11, by increasing distance between reflector and subreflector by more than 25 mm, we start observing multiple focus points that are significantly weaker than a single focal point.

For the EM side-channel detection, presented later in Section V, the focus spot parameters like depth and width play a major role. Focus width, defined in the focal plane, will provide the information of how much area on a chip can be illuminated without the loss of power density. Focus depth on the other hand will provide the measure of the power density variation in the axial direction, which is normal to the chip or board. To measure the focus spot parameters, we use a 3 dB cut-off compared to the point of the highest intensity. The focus width and depth refer to the focus dimension in the xy-plane and along z-axis, respectively. Focus width for the design is 4 mm. Fig. 7, show that the highest intensity region starts at about z = 25 cm and ends at z = 35 cm, giving us a focus depth of 10 cm.

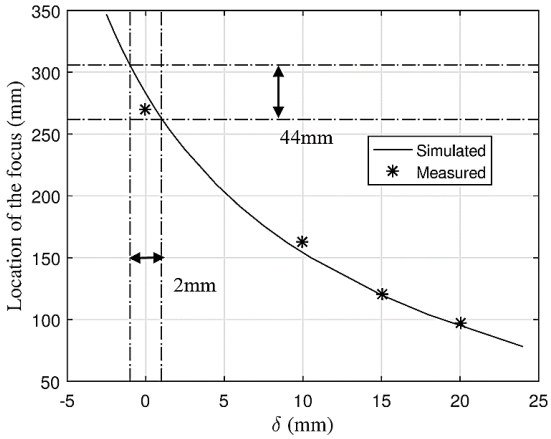

Fig. 10 Location of focus vs subreflector shift.

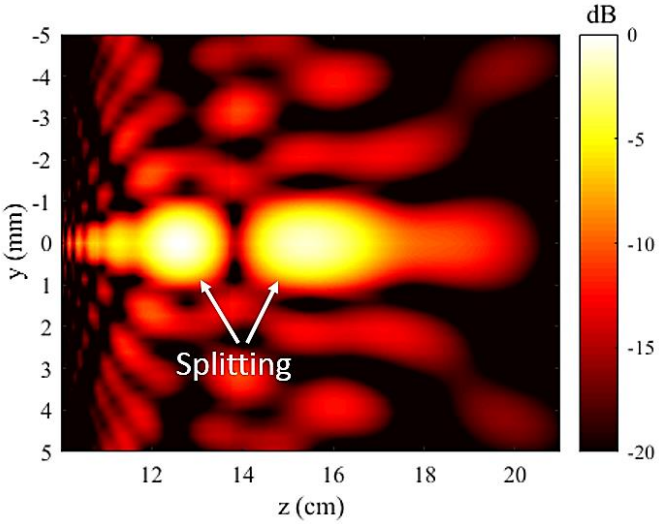

Fig. 11 Focus splitting behavior beyond $\delta = 25$ mm.

The focus depth and width for different subreflector shift values are shown in Fig. 12. It is found that a small shift in the position of the subreflector can have considerable impact on both of the focus parameters. In general, subreflector shifting along the z-axis reduces the size of the focus. Simulation results in Fig. 12 show that focus width decreases from 4 mm to 2 mm as the subreflector shifts by 25 mm from the designed value. Similarly, for the same subreflector shifts, focus depth decreases from 100 mm to 20 mm. This implies that the minimum focus spot size is 2 by 20 mm.

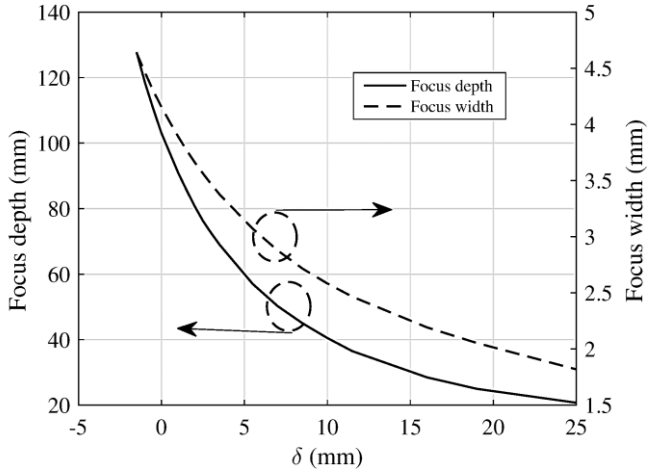

Fig. 12 Simulated focus depth and focus width vs subreflector shift.

The focal parameters variation with subreflector shift can be explained using Gaussian optics as discussed in Sec II. Fig. 13 shows the magnification factor *M* with subreflector shift. It can be seen that *M* decreases with δ and the lowest value converges to the far field configuration *M* of 4.3, which is close to the value obtain using (3). Fig. 14 (a)-(c) compares the calculated values of focus parameters with the full wave simulations. It can be pointed out that for δ<5mm, the calculated values provides good approximation of the focus.

One important factor that introduces inaccuracy to the calculation is the fact that the beam becomes too wide (in terms of angular spread) to be perfectly described by Gaussian optics upon reflecting from the subreflector. Another factor that is not taken into consideration is the calculations of the blockage caused by the subreflector, which degrades the depth and width of focus compared to the idealized Gaussian optics calculation.

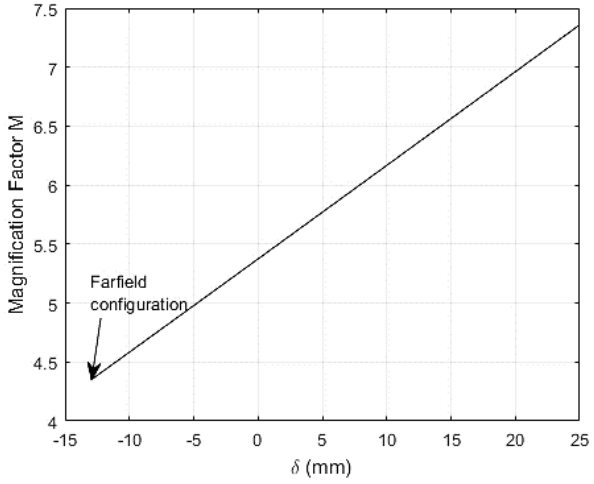

Fig. 13 Magnification factor of the subreflector w.r.t δ.

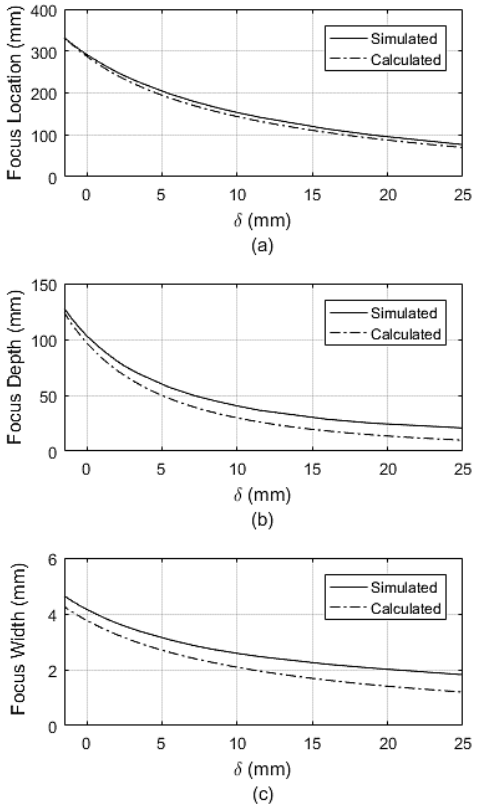

Fig. 14 Comparison of simulated and calculated focus parameters based on Gaussian optics. (a) Focus Location, (b) Focus Depth, (c) Focus Width.

B. Effect of feed position

The feed position, L_f can effect the focus properties. The measurement setup limits the range of L_f as the length of the horn is 22 mm. Simulations were done for the different variation of L_f from it's reference value of 5 mm and the effect on the focus properties were investigated. Fig. 15 show the effect of on the focus location. It shows that the focus from the reference as L_f increases. Fig. 16 shows the effect of feed position on focus depth and width. Focus width changes by 0.6mm and the depth changes by around 25 mm. The range of L_f in these plots are limited by the mechanical constraint of the total length of the horn, on which the reflector is mounted.

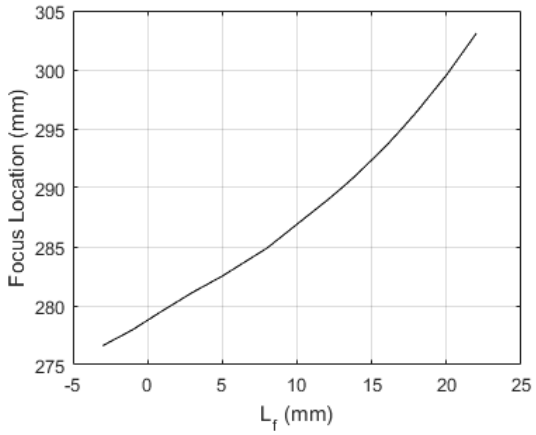

Fig. 15 Focus location vs feed position L_f (default value is 5mm).

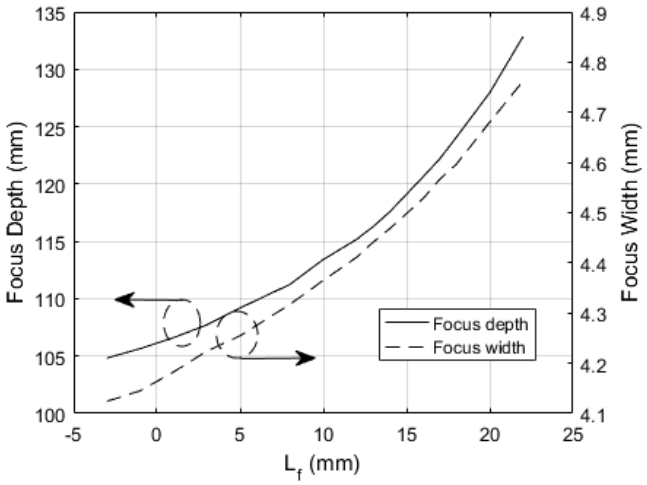

Fig. 16 Focus depth and focus width vs feed position L_f (default value is 5mm).

C. Mutual Coupling Analysis

Since the feed horn use in the near field focused antenna design is high directive source, it is important to analyze the effect of mutual coupling between the horn and the reflector. Feed mismatch, Γ, can be calculated using the stationary phase method as given in [35, eq. (8-30)] where ρ_0 is the distance to the vertex, $G_f(\rho_0)$ the feed gain in the direction of ρ_0, and ρ_1 and ρ_2 the radii of curvature of the reflector at ρ_0.

$$\Gamma = -j\frac{G_f(\rho_0)}{4k\rho_0}\sqrt{\frac{\rho_1\rho_2}{(\rho_1+\rho_0)(\rho_2+\rho_0)}}e^{-j2k\rho_0} \qquad (7)$$

The feed receives the reflected power from the subreflector which results in the mismatch. The simulated reflection coefficient at 300GHz, for the individual horn (without reflector) is -36dB (0.016) as compared -26dB (0.048), when it is used as a feed in the designed reflector antenna configuration.

The coupling effect is also observed in the aperture field of the horn feed. Fig. 17 shows the electric field amplitude over the horn aperture. It can be seen that the aperture field is not changed significantly by the addition of the reflectors. The squared sum error of the entire field distribution is 0.05, which confirms that the mutual coupling does not have a significant effect on the aperture field distribution.

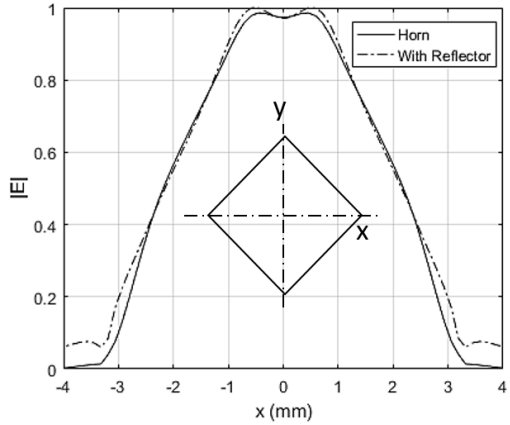

Fig. 17 Simulated aperture field of the horn with and without reflector

IV. Fabrication and Measurements

The antenna geometry shown in the Fig. 3 was designed, fabricated and tested. The antenna is fabricated using 3D printing technology. A type of nylon, PA2200, was used to fabricate the main reflector, the subreflector and the struts. The geometrical parameters for the fabrication have been listed in Table I.

A. Fabrication

The antenna has a main reflector and a small subreflector, which can be fabricated using lathe. Here, instead of that we used 3D printing technique for the fabrication of both the reflectors and struts. 3D printing allows for a cheap and fast prototype manufacturing that is precise and easy to modify. Below, we explain how the 3D printed plastic is treated to function as a metallic reflector.

3D printers slice the model into thin stacked layers along the z-axis. Therefore, an important measure of quality for 3D printing is the layer thickness. Since curved features along the z-axis will show a staircase approximation in the finished prototype, working with smaller layer thickness will results in a more accurate product. The printer that was used, FORMIGA P 110, has a layer thickness of 0.06 mm; which would be very accurate for the lower end of the mm-wave range. However, for the THz frequency range operation (300 GHz), small imperfections on the reflector surfaces lead to phase error losses and can significantly affects the performance parameters like focused directivity. For this reason, additional smoothing had to be applied to the surface of the reflectors.

Prior to smoothing the surface by sanding, a thin single coat of a wet sandable automobile primer was applied to the surface. This primer provides a surface that is easier to smooth, and easier for the conductive paint to adhere to. After that, the surface was smoothed using first 600 then 1200 grit sanders. It is very important to use gentle methods or instruments in this process so as not to change the geometry of the reflector and only remove the nonidealities of the printer.

The smoothed surface becomes ready for the conductive paint to be applied. The particular conductive paint that was used here is MG Chemicals silver paint. There are many different brands of conductive paints with several methods of application. The most convenient products would be aerosol cans; however, for this prototype 0.2 mm nozzle airbrush was used to spray pure silver paint on the prototype at a 20 cm distance to get uniform coating. This method allows for greater control over how the paint is dispersed and ensures the best quality of surface conductivity. The outlined method resulted in a conductive surface that very well matched the simulations using perfectly smooth PEC surfaces.

The second significant design choice was the struts. For this prototype, four replaceable struts were used to suspend the subreflector. The greatest benefit of these struts is that different sets of struts can be used to hold the subreflector at varying distances away from the subreflector. The same reflector system can switch from a far field antenna configuration to a near field focus configuration manually in under a minute. Moreover, struts of varying lengths can be used to further tune

the location of the near field focus as shown in Fig. 12, a technique that was used in this paper. We have manufactured three different lengths of struts as shown in Fig. 18. Some applications could potentially utilize asymmetrical struts to hold the subreflector at an angle to change the beam direction, but this was not investigated in this paper.

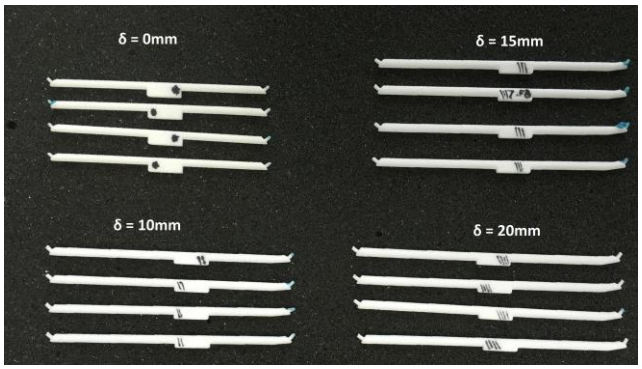

Fig. 18 Sets of struts of different sizes.

There are many other ways to suspend a subreflector in front of a main reflector. The fact that the reflector system can be easily assembled and disassembled becomes very convenient when the reflector surfaces are smoothed and painted. If the entire reflector system was a single piece, the pieces would have been more rigidly aligned (e.g. if replaceable struts are used in a vibrating system, the alignment might degrade as time goes on); however, the reflector surfaces would be much more difficult to reach for even smoothing and painting. The main reflector has a 9mm square hole in it to fit onto a diagonal feed horn of the measurement system. The reflector can be used with a less or more directive feeds; all that is necessary is to adjust the square hole size in the main reflector so that it will fit securely onto the feed-horn. The final form of the reflector is show in Fig. 19.

B. Measurements

The measurement setup consists of the N5224A vector network analyzer (VNA), the VDI transmitter (Tx210), and the VDI receiver (Rx148). In the transmitter, the THz-range carrier signal starts out as a 25-GHz signal, which is generated by a Herley-CTI phase-locked dielectric resonator [38]. This signal is amplified, and its frequency is doubled using Norden N08-1975 [39]; and then, its frequency is tripled using VDI WR6.5X3 [40].This signal is then fed to a subharmonic mixer (WR2.8SHM [41]) that plays a dual role of doubling the carrier frequency and mixing it with the baseband input signal (delivered by the VNA). The THz-range signal is then transmitted by the horn antenna that has a gain of 25 dBi in the range of operation. At the receiver side, the same components are used to downconvert the signal. The final signal is fed back to the VNA and the transfer parameter S_{21} results are calibrated. The measurement section in [42] describes the Tx-Rx system in even more detail. The transceiver system with the designed antenna on transmitter and horn on the receiver is shown in Fig. 20. This system was then placed on a perpendicular set of dovetail optical rails on an optical breadboard to cover the entire 2D plane. The system was elevated from the ground plane (the optical breadboard) using 25.4 mm and 152.4 mm poles as shown in Fig. 21

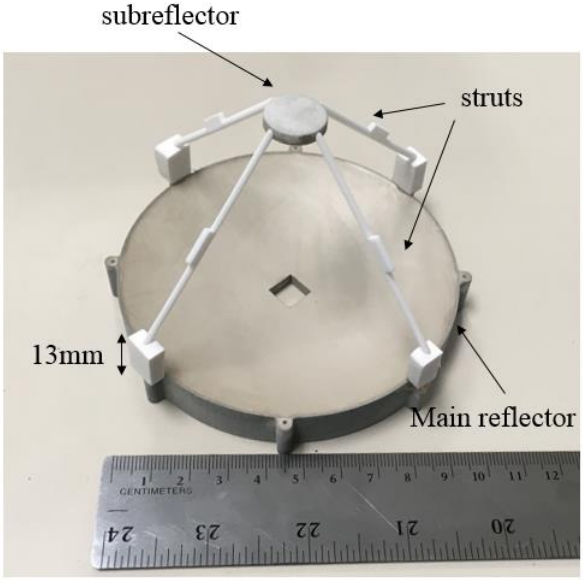

Fig. 19 The silver coated and assembled reflector (without feedhorn).

The designed reflector itself has a very wide bandwidth, for this reason its frequency performance parameters are only affected by the feed diagonal horn and the transmitter. The bandwidth of the diagonal horn is 260GHz-400GHz and the bandwidth of the transmitter is 300GHz-320GHz.

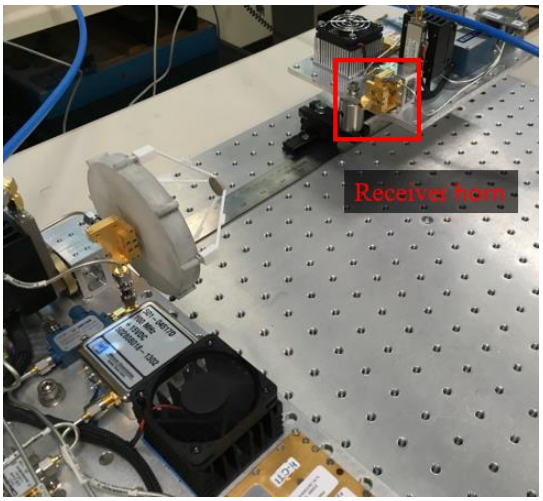

Fig. 20 The Tx-Rx system with the reflector on the Tx side.

Proximity of the antennas to the ground plane is not a concern in this setup as the focused beam has narrow first null beamwidth and hence will not reflect from the ground for the given heights used in measurements. This has been thoroughly validated by measurements. In addition, there is negligible difference between an elevation of 25.4 mm and 152.4 mm. Measurements were done along the axial coordinate, which is the z-axis, and in the transverse xy-plane (focal plane). As shown in Fig. 18, struts of different lengths were fabricated. These struts can be swapped to fine tune δ, the relative position of the subreflector. From the study done in the previous section,

the location and the size of the focus is sensitive to δ, and hence experimental validation for different values is meaningful.

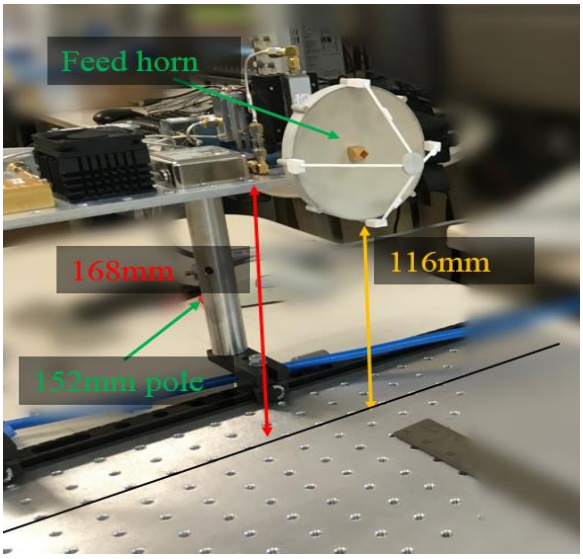

Fig. 21 Height of the focusing antenna from the ground plane.

First, the relative power density was measured in the focal plane to check the focal spot width. The relative power density in the focal plane is shown in the Fig. 22. The measured focus width (3 dB width) is around 4 mm, as shown in the Fig. 22.

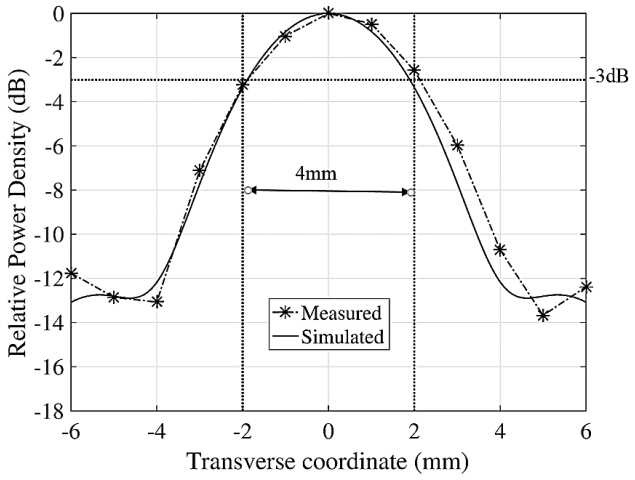

Fig. 22 Relative power density in the focal plane.

Fig. 23 shows the simulated and the measured power density of the designed antenna along its axis. In these plots, separation distance d is the axial distance measured from the secondary reflector, which is located at (0,0). Measured results agree very well with the simulated results. Upon de-embedding the losses in the cables and the transceiver system, we observe ~0.7 dB which is the result of the nylon struts, conductor loss, and the surface roughness loss of the silver paint. The loss analysis is discussed in detail, later in Secion IV-C. Fig. 23 (a) shows that for δ= 0 mm, the 3 dB focus depth is 97 mm, with maximum at 27 cm. Upon moving the subreflector 10 mm, i.e for δ= 10 mm, the focus depth reduces to 39mm and the position of the maximum moves 11 cm closer. Similarly For δ= 15 mm and 20 mm; the focus depth reduces to 30 mm and 25 mm respectively; maximum moves 15 cm and 18 cm closer respectively.

To evaluate the overall performance of the nearfield focuser, we use the focus antenna gain, similar to the focus antenna directivity defined in [29]. This parameter essentially compares the field intensity of the near field focused antenna at the exact location of the focus to the field intensity an isotropic source would have created at the same distance. In other words, the field created by our reflector antenna at a distance of 28 cm is 46 dB stronger than the field created by an isotropic source at a distance of 28 cm.

This is further validated with a gain transfer measurement using 2 identical horn antennas with 25 dBi gain. S_{21} power transmission with a separation distance of 28 cm was observed to be 21 dB stronger for Reflector-to-Horn setup compared to the Horn-to-Horn setup. This is also confirmed by the side channel detection measurements shown in the next section.

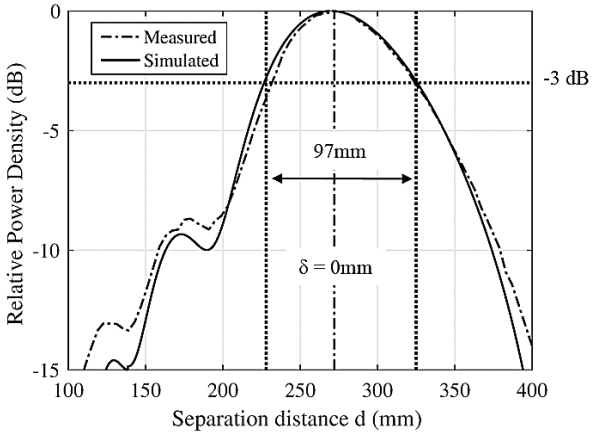

(a)

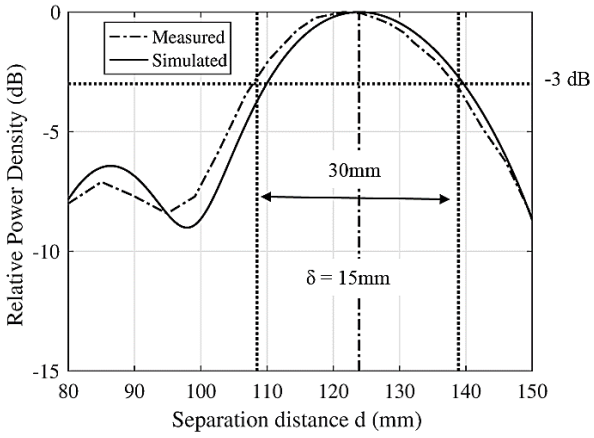

(c)

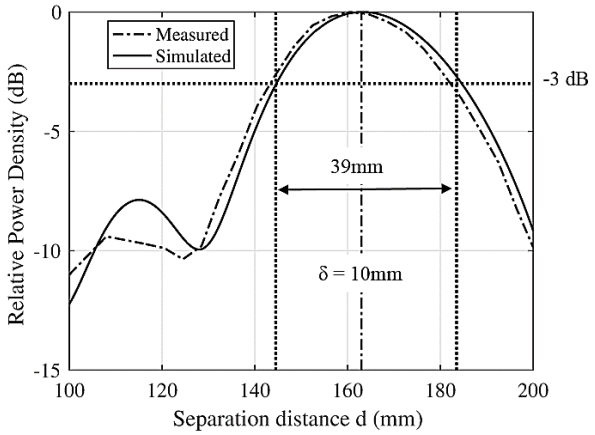

(b)

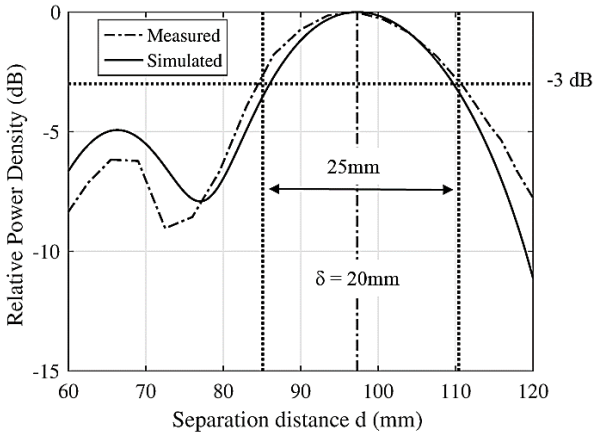

(d)

Fig. 23 Simulated and measure relative power density of the prototype shown in Fig. 20 along the z-axis.

C. Loss analysis

At THz frequencies, the primary contributor to the loss in the antenna configuration is caused by surface roughness of the conducting material used in the fabrication. The roughness loss depends upon the variation in surface height. In practice, standard smoothing techniques such as polishing can be applied to minimize this loss. Fig. 24 shows simulated and theoretical roughness loss w.r.t standard deviation of surface height for the designed reflector antenna. The theoretical loss is calculated using (8) [43].

$$\exp\left[-\left(\frac{4\pi\sigma_s}{\lambda}\right)^2\right] \qquad 8)$$

The fabricated prototype was measured to have an RMS surface roughness of 4 µm, which results in less than 0.1 dB loss.

Another source of loss is the imperfect conductivity of the silver paint. The effect conductivity has on the loss is shown in Fig. 25. The datasheet for the MG Chemicals Liquid silver paint, used in prototype, has a conductivity value of 0.5 MS/m, which results in 0.15 dB loss.

Struts loss in investigated for the different struts size and is shown in Fig. 26. For the fabricated prototype the struts diameter of 1.5mm is selected, which results in 0.3 dB loss.

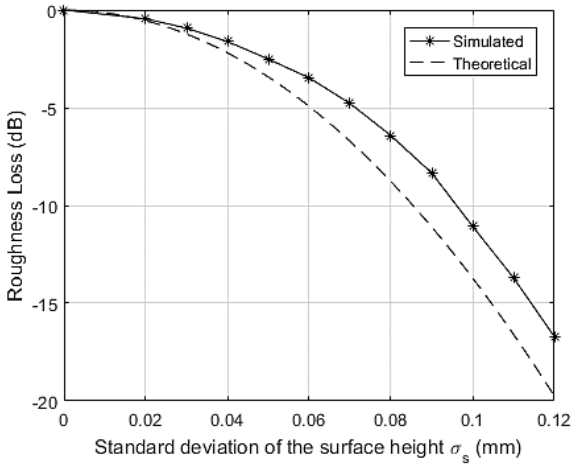

Fig. 24 Loss due to the roughness of the surface.

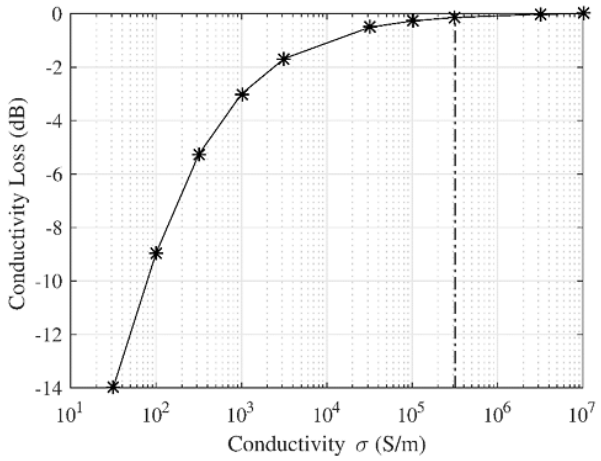

Fig. 25 Simulated loss due to the conductivity of the paint.

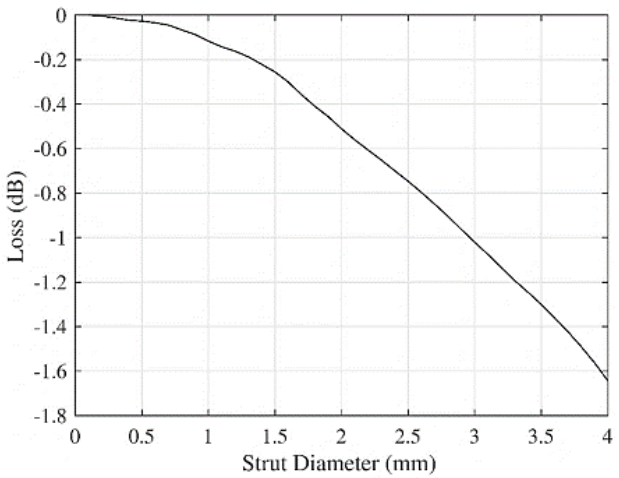

Fig. 26 Simulated loss due to the obstruction of the struts.

Measurements shows 0.7dB total loss compared to the ideal PEC cassegrain; which is a contribution of surface roughness, conductivity and strut losses. The remaining 0.7-0.5 = 0.2dB is likely a result of measurement uncertainty and miniscule imperfections in alignment.

V. Near Field Focuser In Backscatter Side-Channel Application

In this section, we conduct backscatter side-channel measurements to demonstrate the performance of our proposed THz near field focuser. The goals are to show that the proposed near field focuser can effectively amplify the received backscatter signal and increase distance range, which are of critical importance due to THz (300 GHz) signal's high attenuation with distance. The backscatter side-channel is created by switching activity of transistors in digital electronic circuits, such as microprocessors [19]. We have implemented a four-bit RFID design as described in [19] in Altera DE0-Cyclone V FPGA, and demonstrated that the message can be read from outside of the FPGA board via backscatter side-channel. Details of circuit designs can be found in [19].

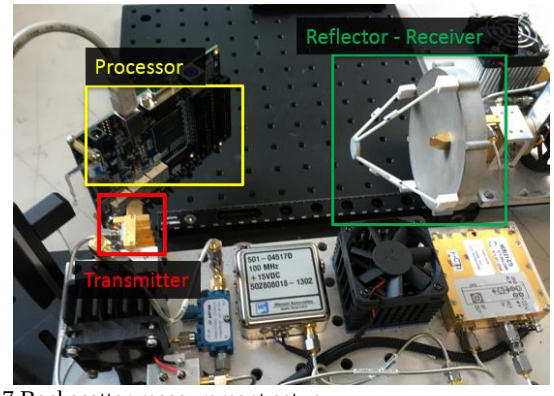

Fig. 27 Backscatter measurement setup.

Fig. 27 presents our backscatter measurement setup. An Agilent MXG N5183A Signal Generator with input power of 15 dBm is used as a signal source and an Agilent MXA N9020A Vector Signal Analyzer is used to record the backscatter signals. An Altera DE0-Cyclone V FPGA board is used as an electronic device that generates backscatter side-channel.

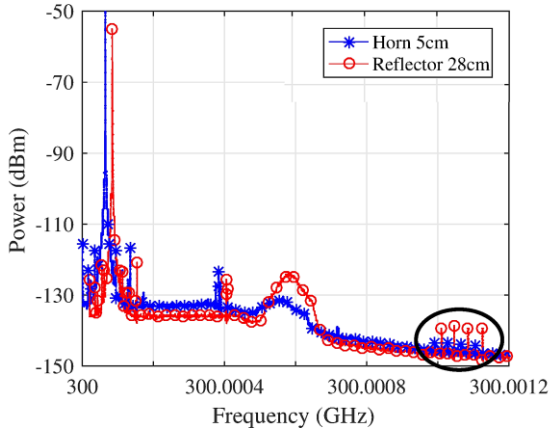

Fig. 28 Measured spectrums of the 4bits backscatter signals at 300 GHz.

Fig. 28 presents the measured spectrum of the 4 bits backscatter signal at 300 GHz. The blue curve is the measurement result with standard gain horn antennas at a Tx-Rx distance of 5 cm and the red curve is the measurement result with the near field focuser at a Tx-Rx distance of 28 cm. A relatively strong carrier signal is observed at around 300 GHz and all four modulated backscattered peaks are observed at around 1 MHz away from the carrier frequency. Note that a hump at around 600 kHz away from the carrier frequency is observed in Fig. 28. This hump is caused by the THz transceivers, which is not of interests in this paper.

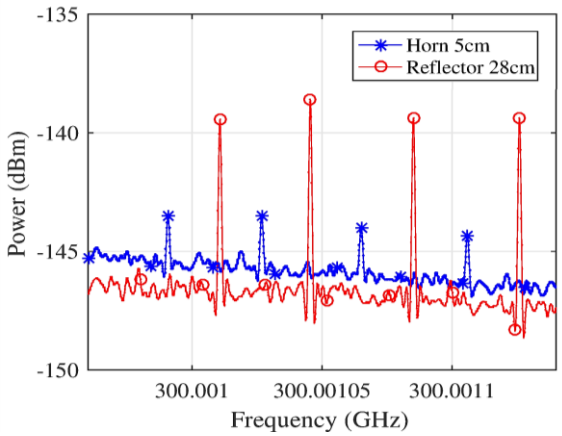

Fig. 29 Measured spectrums of the 4 bits backscatter signals at 300 GHz; zoom-in of the modulated signals.

Fig. 29 shows a closer look at the modulated backscatter signals. It is observed that the received backscattered power with the near field focuser is around 6 dB stronger than the power without the near field focuser at a distance that is almost six times farther (28 cm versus 5 cm). This means the reflector overcomes the extra 15 dB pathloss (28 cm vs 5 cm separation distance) and still delivers 6 dB more power. These power levels further validate our measured focused antenna gain value of 46 dBi. This is explained as follows:

Increase in received power + Path loss difference
+ Gain of the feed horn
= Focused Antenna Gain

$$6\ \text{dB} + 15\ \text{dB} + 25\ \text{dBi} = 46\ \text{dBi}$$

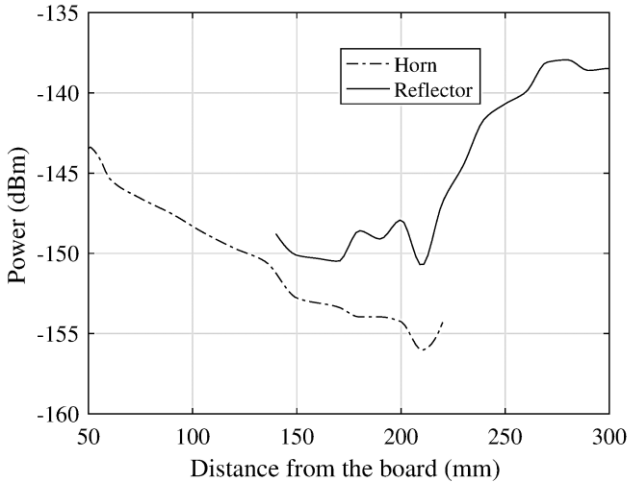

Fig. 30 Received backscattered power level with respect to the Rx-to-FPGA board distance.

In Fig. 30 we compare the averaged received power levels of a single bit obtained from the horn antenna and the manufactured reflector at distances from around 5 cm to 30 cm. It is observed that with the use of the horn antenna, the received backscattered power (dotted curve in Fig. 30) gradually decreases as distance increases from 5 cm to 22 cm. At distance beyond 22 cm, the backscattered signal is no longer observable since it decays below the noise floor. In contrast, with the near field reflector, the received power (solid curve in Fig. 30) reaches a maximum value at around -138 dBm as distance approaches 28 cm.

VI. Conclusion

Backscatter side channel detection using THz near field focusing was presented in this paper. THz near field focusing allows the backscatter signal to detect at larger distances as compared to the far field radiator. The cassegranian reflector configuration was used to design the focused antenna. The sensitivity of the focus parameters like focus depth and width w.r.t. the subreflector small shifts were investigated. It is found that 1 mm change in the subreflector position can shift the focal plane by 2 cm. The relative power density along the axis for the various struts sizes were studied and it is found that the 3 dB focus depth decreases with increase in struts size. The focused antenna was fabricated using 3D printing technology, which facilitates rapid prototyping. Metallization of the reflector surfaces were done using conductive silver paint. Finally, we presented the backscatter signal detection using the designed antenna and it was shown that the designed antenna can detect the signal 28 cm farther from the board aperture as compare to the far field antenna.

References

[1] P. Kocher, J. Jaffe, and B. Jun, "Differential power analysis: leaking secrets," in *Proceedings of CRYPTO'99, Springer, Lecture notes in computer science*, 1999, pp. 388–397.

[2] A. G. Bayrak, F. Regazzoni, P. Brisk, F.-X. Standaert, and P. Ienne, "A first step towards automatic application of power analysis countermeasures," in *Proceedings of the 48th Design Automation Conference (DAC)*, 2011.

[3] U. R¨uhrmair, X. Xu, J. S¨olter, A. Mahmoud, M. Majzoobi, F. Koushanfar, and W. Burleson, "Efficient power and timing side channels for physical unclonable functions," in *International Workshop on Cryptographic Hardware and Embedded Systems*. Springer, 201.

[4] M. Backes, M. Durmuth, S. Gerling, M. Pinkal, and C. Sporleder, "Acoustic side-channel attacks on printers," in *Proceedings of the USENIX Security Symposium*, 2010.

[5] S. Chari, J. R. Rao, and P. Rohatgi, "Template attacks," in *Proceedings of Cryptographic Hardware and Embedded Systems - CHES 2002*, 2002, pp. 13–28.

[6] D. Agrawal, B. Archambeult, J. R. Rao, and P. Rohatgi, "The EM sidechannel(s)," in *Proceedings of Cryptographic Hardware and Embedded Systems - CHES 2002*, 2002, pp. 29–45.

[7] L. Batina and M. Robshaw, *Cryptographic Hardware and Embedded Systems - CHES 2014 16th International Workshop, Busan, South Korea, September 23-26, 2014. Proceedings*. Berlin: Heidelberg, 2014.

[8] M. G. Khun, "Compromising emanations: eavesdropping risks of computer displays," The complete unofficial TEMPEST web page: http://www.eskimo.com/˜joelm/tempest.html, 2003.

[9] A. Zajic and M. Prvulovic, "Experimental demonstration of electromagnetic information leakage from modern processor-memory systems," *Electromagnetic Compatibility, IEEE Transactions on*, vol. 56, no. 4, pp. 885–893, Aug 2014.

[10] D. Genkin, L. Pachmanov, I. Pipman, and E. Tromer, "Stealing key from pcs using a radio: Cheap electromagnetic attacks on windowed exponentiation," in *International Workshop on Cryptographic Hardware and Embedded Systems*. Springer, 2015, pp. 207–228.

[11] Y. Hayashi *et al*., "Efficient Evaluation of EM Radiation Associated With Information Leakage From Cryptographic Devices," in *IEEE Transactions on Electromagnetic Compatibility*, vol. 55, no. 3, pp. 555-563, June 2013..

[12] R. Callan, A. Zajic, and M. Prvulovic, "A practical methodology for measuring the side-channel signal available to the attacker for instruction-level events," in *Microarchitecture (MICRO), 2014 47th Annual IEEE/ACM International Symposium on*. IEEE, 2014, .

[13] M. Prvulovic, A. Zajic, R. L. Callan, and C. J. Wang, "A method for finding frequency-modulated and amplitude-modulated electromagnetic emanations in computer systems," *IEEE Transactions on Electromagnetic Compatibility*, vol. 59, no. 1, pp. 34–42, Feb 201.

[14] R. Callan, F. Behrang, A. Zajic, M. Prvulovic, and A. Orso, "Zerooverhead profiling via em emanations," in *Proceedings of the 25th International Symposium on Software Testing and Analysis. ACM*, 2016, pp. 401–412.

[15] N. Sehatbakhsh, A. Nazari, A. Zajic, and M. Prvulovic, "Spectral profiling: Observer-effect-free profiling by monitoring em emanations," in *Microarchitecture (MICRO), 2016 49th Annual IEEE/ACM International Symposium on*. IEEE, 2016, pp. 1–11.

[16] A. Nazari, N. Sehatbakhsh, M. Alam, A. Zajic, and M. Prvulovic, "Eddie: Em-based detection of deviations in program execution," in *Proceedings of the 44th Annual International Symposium on Computer Architecture, ser. ISCA '17*, 2017, pp. 333–346.

[17] D. Agrawal, S. Baktir, D. Karakoyunlu, P. Rohatgi and B. Sunar, "Trojan Detection using IC Fingerprinting," *2007 IEEE Symposium on Security and Privacy (SP '07)*, Berkeley, CA, 2007, pp. 296-310.

[18] C. He, B. Hou, L. Wang, Y. En and S. Xie, "A failure physics model for hardware Trojan detection based on frequency spectrum analysis," *2015*

IEEE International Reliability Physics Symposium, Monterey, CA, 2015, pp. PR.1.1-PR.1.4.

[19] C.-L. Cheng, L. N. Nguyen, M. Prvulovic, and A. Zajic, “Exploiting switching of transistors in Digital electronics for RFID tag design,” *IEEE International Conference on RFID*, pp. 1-2, April 2018, Orlando FL.

[20] Y. J. Cheng and F. Xue, "Ka-Band Near-Field-Focused Array Antenna with Variable Focal Point," in *IEEE Transactions on Antennas and Propagation*, vol. 64, no. 5, pp. 1725-1732, May 2016.

[21] H. D. Hristov and M. H. A. J. Herben, "Millimeter-wave Fresnel-zone plate lens and antenna," in *IEEE Transactions on Microwave Theory and Techniques*, vol. 43, no. 12, pp. 2779-2785, Dec 1995.

[22] S. Karimkashi, A. A. Kishk, "Focusing properties of Fresnel zone plate lens antennas in the near-field region", *IEEE Trans. Antennas Propag*., vol. 59, no. 5, pp. 1481-1487, May 2011.

[23] P. F. Li, S. W. Qu, S. Yang and Z. P. Nie, "Microstrip Array Antenna With 2-D Steerable Focus in Near-Field Region," in *IEEE Transactions on Antennas and Propagation*, vol. 65, no. 9, pp. 4607-4617, Sept. 2017.

[24] L. Shan and W. Geyi, "Optimal Design of Focused Antenna Arrays," in *IEEE Transactions on Antennas and Propagation*, vol. 62, no. 11, pp. 5565-5571, Nov. 2014.

[25] H. T. Chou, T. M. Hung, N. N. Wang, H. H. Chou, C. Tung and P. Nepa, "Design of a Near-Field Focused Reflectarray Antenna for 2.4 GHz RFID Reader Applications," in *IEEE Transactions on Antennas and Propagation*, vol. 59, no. 3, pp. 1013-1018, March 2011.

[26] H. Kamoda, T. Iwasaki, J. Tsumochi, T. Kuki and O. Hashimoto, "60-GHz Electronically Reconfigurable Large Reflectarray Using Single-Bit Phase Shifters," in *IEEE Transactions on Antennas and Propagation*, vol. 59, no. 7, pp. 2524-2531, July 2011.

[27] S. Shahid and G. G. Gentili, "Shaped horn antenna for spot focusing THz imaging application," *2016 Loughborough Antennas & Propagation Conference (LAPC)*, Loughborough, 2016, pp. 1-4.

[28] M. Zhou, Y. Alfadhl and X. Chen, "Study on a THz image scanning system with ellipsoidal reflector," *2015 8th UK, Europe, China Millimeter Waves and THz Technology Workshop (UCMMT)*, Cardiff, 2015, pp. 1-2.

[29] E. Gandini, A. Tamminen, A. Luukanen and N. Llombart, "Wide Field of View Inversely Magnified Dual-Lens for Near-Field Submillimeter Wavelength Imagers," in *IEEE Transactions on Antennas and Propagation*, vol. 66, no. 2, pp. 541-549, Feb. 2018.

[30] E. Danieli and Y. Pinhasi, "Variable focusing antenna for wireless power transmission and remote sensing at millimeter wavelengths," *2012 IEEE 27th Convention of Electrical and Electronics Engineers* in Israel, Eilat, 2012, pp. 1-1.

[31] L. Shafai, A. A. Kishk, and Sebak, “Near field focusing of apertures and reflector antennas,” in *Proc. IEEE Communications, Power and Computing Conf*., May 22–23, 1997, pp. 246–251.

[32] N. Llombart, K. B. Cooper, R. J. Dengler, T. Bryllert and P. H. Siegel, "Confocal Ellipsoidal Reflector System for a Mechanically Scanned Active Terahertz Imager," in *IEEE Transactions on Antennas and Propagation*, vol. 58, no. 6, pp. 1834-1841, June 2010.

[33] P. -. Kildal and M. M. Davis, "Characterisation of near-field focusing with application to low altitude beam focusing of the Arecibo tri-reflector system," in *IEEE Proceedings - Microwaves, Antennas and Propagation*, vol. 143, no. 4, pp. 284-292, Aug. 1996.

[34] R. C. Hansen, “Focal region characteristics of focused array antennas,” *IEEE Trans. Antennas Propag*., vol. 33, no. 12, pp. 1328–1337, Dec. 1985.

[35] T. Milligan and J. Wiley, Modern Antenna Design. New York NY, USA: Wiley Online Library, 2005.

[36] B. E. A. Saleh, M. C. Teich, Fundamentals of Photonics, New York: Wiley, 1991.

[37] CST, Darmstadt, Germany, 2017. Available: https://www.cst.com/.

[38] [Online]. Available: https://www.ultra-herley.com/uploads/herley/ datasheets/cti/Ultra%20Herley%20Series% 20PDRO.pdf.

[39] [Online]. Available: http://www.nordengroup.com /product-group /frequency-multiplier- 33-to-50-ghz/.

[40] [Online]. Available: http://www.vadiodes.com /en/wr6-5x3.

[41] [Online]. Available: http://vadiodes.com /en /wr2-8shm.

[42] S. Kim and A. G. Zajić, "Statistical Characterization of 300-GHz Propagation on a Desktop," in *IEEE Transactions on Vehicular Technology*, vol. 64, no. 8, pp. 3330-3338, Aug. 2015.

[43] J. Ruze, "Antenna tolerance theory—A review," in *Proceedings of the IEEE*, vol. 54, no. 4, pp. 633-640, April 1966.